ADVANCED FUNCTIONAL MATERIALS
www.afm-journal.de

Blue Luminescence of ZnO Nanoparticles Based on Non-Equilibrium Processes: Defect Origins and Emission Controls

By *Haibo Zeng,* Guotao Duan, Yue Li, Shikuan Yang, Xiaoxia Xu,* and *Weiping Cai*

High concentrations of defects are introduced into nanoscale ZnO through non-equilibrium processes and resultant blue emissions are comprehensively analyzed, focusing on defect origins and broad controls. Some ZnO nanoparticles exhibit very strong blue emissions, the intensity of which first increase and then decrease with annealing. These visible emissions exhibit strong and interesting excitation dependences: 1) the optimal excitation energy for blue emissions is near the bandgap energy, but the effective excitation can obviously be lower, even 420 nm (2.95 eV $< E_g =$ 3.26 eV); in contrast, green emissions can be excited only by energies larger than the bandgap energy; and, 2) there are several fixed emitting wavelengths at 415, 440, 455 and 488 nm in the blue wave band, which exhibit considerable stability in different excitation and annealing conditions. Mechanisms for blue emissions from ZnO are proposed with interstitial-zinc-related defect levels as initial states. EPR spectra reveal the predominance of interstitial zinc in as-prepared samples, and the evolutions of coexisting interstitial zinc and oxygen vacancies with annealing. Furthermore, good controllability of visible emissions is achieved, including the co-emission of blue and green emissions and peak adjustment from blue to yellow.

1. Introduction

As a wide-bandgap semiconductor, wurtzite ZnO – with an exciton binding energy of 60 meV at room temperature (RT), which is larger than those of the widely used semiconductors GaN (26 meV) or ZnSe (20 meV) and also larger than the RT thermal energy (25 meV) – has attracted the attention of researchers for several decades due to its many important applications, especially in optics and optoelectronics.[1–6] Recently, the renewed interest in nanostructured ZnO has been fueled by its attractive prospects for applications including RT nanolasers, p-type doping and RT ferromagnetic semiconductor nanomaterials.[7–13] These prospects have led to extensive studies of many aspects of ZnO nanostructures, including synthesis strategies, physical and chemical properties, and applications.

However, in spite of several decades of effort, some of the basic properties of ZnO still remain unclear.[14,15] In particular, the identification of the dominant intrinsic defects (oxygen vacancies, V_O, interstitial zinc, Zn_i, and hydrogen interstitials, H_i)[16-24] and the origins of the defect-related emissions in the visible region[25–34] have been controversial for quite a long time. The control of intrinsic defects and the corresponding effects on properties is of paramount importance in applications of ZnO. For example, achieving p-type ZnO with sufficient carrier concentration in a reproducible way relies on striking a careful balance between control of extrinsic doping and intrinsic defect concentration.[35,36] Defect studies have been considered for more than 40 years, but now need revisiting in the context of novel applications using nanostructured materials. Moreover, the relationships among defect chemistry, processing and properties has not received much attention.[15]

In the photoluminescence (PL) spectra of ZnO, typically there are emission bands in the ultraviolet (UV) and visible (green, yellow, blue and violet) regions. The UV emission is usually considered as the characteristic emission of ZnO,[37,38] and attributed to the band–edge transition or the exciton combination.[32] Although the emissions in the visible regions are universally considered to be associated with the intrinsic or extrinsic defects in ZnO, extensive controversies have existed for more than two decades on the clear defect centers, and unambiguous electron transitions are not yet known in detail.[39] For green emissions, a number of different hypotheses have been proposed, such as transition between singly ionized oxygen vacancies and photoexcited holes,[25] transition between electrons close to the conductive band and deeply trapped holes at V_O^{++},[26] surface defects,[31] etc. The yellow-orange emissions have been assigned to interstitial oxygen and dislocation, as well as Li dopants.[14]

Here, we focus on the origins and controllability of blue emissions of ZnO nanoparticles. Due to ZnO's good electric parameters, avirulence and biological compatibility, the blue

[*] Prof. H. Zeng, Dr. G. Duan, Dr. Y. Li, Dr. S. Yang, Dr. X. Xu, Prof. W. Cai
Key Laboratory of Materials Physics
Anhui Key Laboratory of Nanomaterials and Nanotechnology
Institute of Solid State Physics
Chinese Academy of Sciences
Hefei 230031 (P. R. China)
E-mail: hbzeng@issp.ac.cn

DOI: 10.1002/adfm.200901884

luminescence of ZnO nanoparticles would have potential in visible light emission and biological fluorescence labeling applications. However, blue and violet emissions of ZnO have previously been highly undesirable, and the few reported emissions were very weak in intensity.[40–42] Thus, the biggest problems for the blue emissions of ZnO are the unknown mechanisms, weak intensity and poor controllability.

In this paper, strong blue emissions were observed from ZnO nanoparticles based on non-equilibrium processes, including laser ablation-induced extreme conditions[43,44] and zinc-rich annealing. Comprehensive spectral studies, including the effect of annealing and excitation, were implemented on these blue emissions. Furthermore, the PL excitation (PLE) spectra and electron paramagnetism (EPR) spectra were used to analyze the features of excited states and related defects. As a result, the blue emissions were attributed to the transitions involved in zinc interstitials. Moreover, according to the built mechanisms, good controllability was achieved, including the co-emission of blue and green emissions, and adjustment of the emitting wavelength from blue to yellow regions. This study may deepen the understanding of defect-related emissions in ZnO, and extend the optic and optoelectronic applications of ZnO nanostructures.

2. Results and Discussion

2.1. Structure Characterizations and Blue Emissions

In this study, ZnO nanoparticles produced highly non-equilibrium processes – including laser ablation in liquid (LAL)[43,44] and subsequent zinc-rich annealing – were selected as model materials to investigate the origin and controllability of the blue emissions of ZnO. When a laser beam with energy higher than the ablation threshold acts on a solid zinc target in the liquid, the interaction will instantaneously produce a plasma at high temperature, high pressure and a high concentration (HTHPHC) of highly excited species.[45] Another special condition should be noticed: the composition of plasma is remarkably zinc-enriched. Furthermore, the formation of nanoparticles is very fast due to the huge temperature difference between the hot plasma and the surrounding liquid medium. As predicted by Hagemark's defect reaction constants, the equilibrium concentrations of various defects will exponentially increase with temperature if we suppose that the formation of defects be in equilibrium states at every instant time with fixed temperature.[16,46] The high concentration of defects formed at high temperature will be rapidly ''frozen'' in the ZnO lattice due to the ultrafast quenching of hot plasma by the surrounding liquid medium. Ischenko's recent results also demonstrated that the higher the formation rate of ZnO nanocrystal, the more defective it is.[47] These three factors, including HTHPHC conditions, Zn-richness, and rapid formation rate, lead the growth thermodynamics of nanoparticles to deviate greatly from the equilibrium states. Thus, the non-equilibrium processes can induce a high concentration of special defects, which is beneficial to the study of visible luminescence.

In principle, there are a number of defect states within the bandgap of ZnO. The donor defects are $Zn_i^{\bullet\bullet}$, $Zn_i^{\bullet}$, Zn_i^{X}, $V_O^{\bullet\bullet}$, $V_O^{\bullet}$ and V_O, and the acceptor defects are V''_{Zn} and V'_{Zn}.[14,15] Zn interstitials and oxygen vacancies are known to be the predominant ionic defect types.[18,20–22] The former are shallow donors, while oxygen vacancies create deep levels.[20,22,26] Other types of point defects, such as V_{Zn} and O_i may also be thermodynamically stabilized in the ZnO crystal lattice, but at higher oxygen partial pressure.[48] However, which defect (Zn_i or V_O) dominates in native, undoped ZnO is still a matter of great controversy. Zn interstitials come from the Frenkel reaction, Equation (1), and further ionization reactions, Equation (2) and (3), while the oxygen vacancies arise from the Schottky reaction, Equation (4), and further ionization reactions, Equation (5) and (6). From these defect reactions, it can be seen that the both kinds of defects donate two electrons, and thus it is difficult to distinguish one from the other using electrical measurements.

$$\mathrm{Zn_{Zn}} \Leftrightarrow \mathrm{Zn}_i^X + \mathrm{V}_{\mathrm{Zn}}^X \quad (1)$$

$$Z_i^X \Leftrightarrow \mathrm{Zn}_i^{\bullet} + e' \quad (2)$$

$$\mathrm{Zn}_i^{\bullet} \Leftrightarrow \mathrm{Zn}_i^{\bullet\bullet} + e' \quad (3)$$

$$0 \Leftrightarrow \mathrm{V}_{\mathrm{Zn}}^X + \mathrm{V}_{\mathrm{O}}^X \quad (4)$$

$$\mathrm{V}_{\mathrm{O}}^X \Leftrightarrow \mathrm{V}_{\mathrm{O}}^{\bullet} + e' \quad (5)$$

$$\mathrm{V}_{\mathrm{O}}^{\bullet} \Leftrightarrow \mathrm{V}_{\mathrm{O}}^{\bullet\bullet} + e' \quad (6)$$

Figure 1a shows the XRD pattern of as-prepared nanoparticles and its evolution with air annealing. For the as-prepared nanoparticles, two sets of diffraction peaks can be observed, belonging to metal Zn and wurtzite ZnO crystals. With increasing annealing temperature, ZnO diffraction peaks increase while Zn peaks decrease, clearly demonstrating the oxidation of Zn. To check the change of ZnO lattice with annealing, normal Si powder was mixed into ZnO nanoparticles for calibration. The mixed XRD patterns in Figure 1b show the obvious deviation of ZnO(100) diffraction peaks from the normal value. This could be the result of high concentration of defects inside the formed ZnO lattice; the reduction of these deviations indicates the relaxation of defects induced by annealing. Figure 1c presents the change of lattice parameter *a* wurtzite ZnO with annealing temperature. Interestingly, the values all are above that expected for an ideal ZnO lattice. The deviation is obviously reduced by annealing, especially the high temperature annealing, but it remains at a high level in the as-prepared and low temperature annealed samples.

TEM examinations in Figure 2a, b and c have revealed that the as-prepared nanoparticles are of Zn-core–ZnO-shell structure. It is worthy noticing that the shell layers contain many ultrafine crystalline ZnO grains, with many disordered areas surrounding them. This is in agreement with our previous results and indicates that there could be a high concentration of defect in the ZnO layers. After high temperature annealing, as shown in Figure 2d, almost all particles are converted into pure and highly crystalline ZnO particles. This coincides with the XRD evolutions in Figure 1.

These structural features indicate that the as-prepared ZnO nanoparticles are rich in some kind of defect produced by non-

equilibrium process, and such defects are sensitive to temperature and can only withstand low temperature annealing.[47] Recently, Vlasenko et al. showed experimentally that interstitial zinc is a very instable defect, but the oxygen vacancy is stable to around

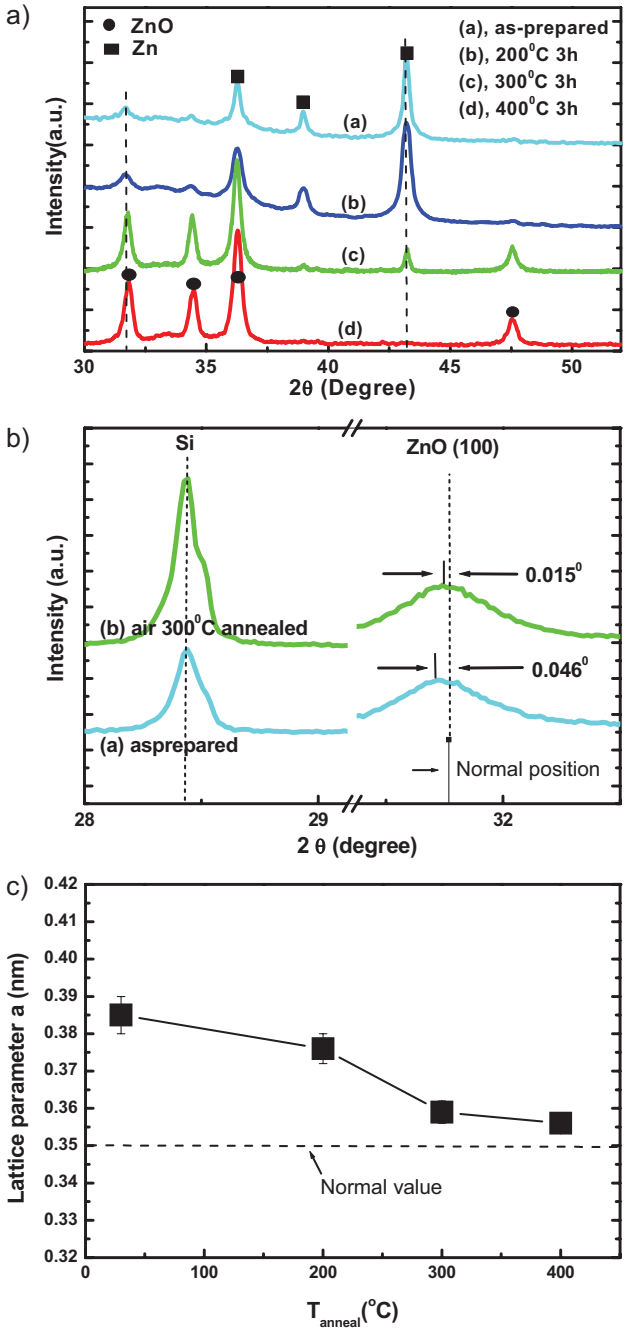

Figure 1. a) XRD patterns of as-prepared and air-annealed ZnO nanoparticles; the dashed lines at ZnO(100) and Zn(001) indicate the composition evolution from Zn/ZnO to ZnO. b), Comparison of ZnO(100) peaks before and after annealing with Si(001) as calibration; the departure of ZnO(100) demonstrates the defect-induced lattice expansion, which is larger in the as-prepared sample. c) Changes of the *a* axis of ZnO with annealing temperature.

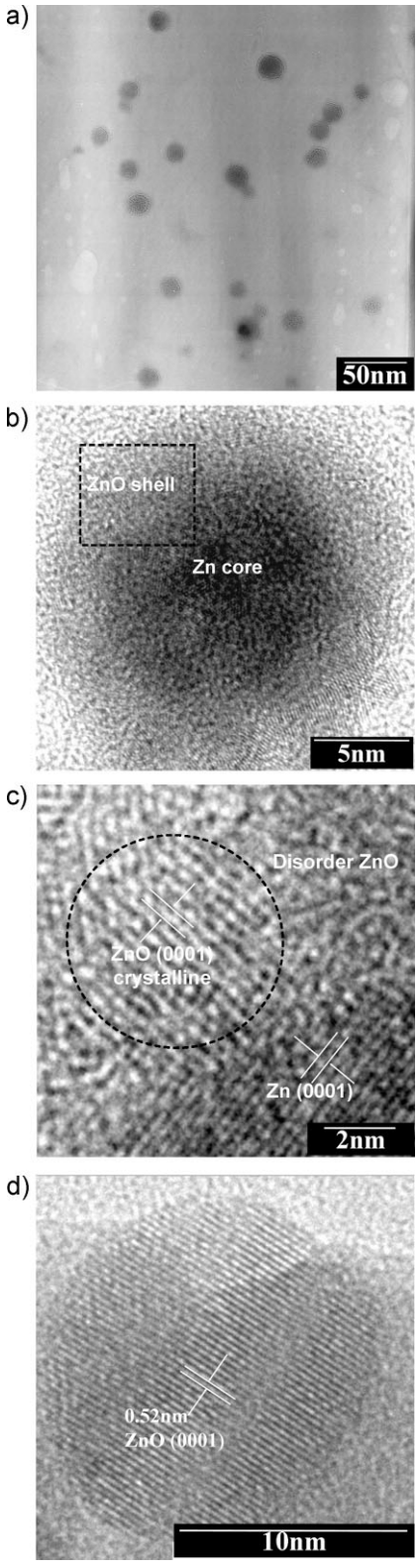

Figure 2. TEM (a) and HRTEM (b and c) images of as-prepared ZnO nanoparticles, showing the core-shell structure and partial disordered microstructure in the shells, and HRTEM images (d) of nanoparticles annealed at 400 °C in air.

400 °C.[49] These experiment results are in agreement with Janotti and Van de Walle's calculation results that zinc interstitials are fast diffusers with a migration barrier as low as 0.57 eV, while that for oxygen vacancies is in the range 1.7 to 2.4 eV.[50]

Because of the different ionization energies, approximately in the range 0.05 to 2.8 eV,[49] the relative concentrations of the various defects depend strongly on formation temperature. However, the partial pressure of oxygen and zinc, pO_2 and pZn, respectively, are also very important.[16,18] Under very reducing conditions and at high temperatures, oxygen vacancies may predominate.[16] Depending on the relative pO_2/pZn ratio, Zn intersitials are the predominant defects under Zn vapor-rich environments. Halliburton et al. implemented annealing of ZnO crystals in zinc vapor at 1100 °C, and then observed formation of zinc interstitials by EPR spectra.[51,52] According to Ba rouwer diagram of ZnO, at low pO_2 and high pZn, it is probable that Zn interstitials dominate, whereas at low pO_2 and low pZn, it is probable that oxygen vacancies dominate.[53,54] Therefore, the highly non-equilibrium processes used in this work, including low pO_2 and high pZn, could produce high content of defects and Zn interstitials could be predominant in the formed ZnO nanoparticles.

Figure 3 presents the typical blue PL of these ZnO nanoparticles and its evolution with annealing. All the spectra were excited by the optimal excitation wavelength. The as-prepared ZnO nanoparticles exhibit a remarkable blue emission with peak at 440 nm. The anneal effects on such blue emissions are very interesting. The peak position of the blue emissions slightly red-shifts from 440 to 455 nm on annealing in air (Fig. 3a), while it remains almost the same on annealing in N_2 (Fig. 3b). However, a giant enhancement of about 100 times is observed for the intensity of blue emissions in both cases. Such an enhancement could be induced by the oxidation of Zn cores, which quench the excited states at the metal–semiconductor interfaces,[4] and the evolution of defect states described below. Compared with previous reports, such strong blue emissions are very infrequent.[42,55–57] After high temperature annealing, the usual band-edge emission in the UV band and deep-level emission in the green band can be seen, as shown in Figure 3c. This corresponds to the highly crystalline ZnO particles, according to the XRD and TEM results in Figure 1 and 2. The dependence of the intensity of blue emissions on annealing temperature is clearly plotted in Figure 3d, from which the rapid increase of intensity under low temperature annealing and sharp quenching under high temperature annealing are both well demonstrated.

Combining the above results and analyses, we can form a temporary hypothesis that the blue emission of ZnO nanoparticles could originate from transitions involving Zn interstitial defect states. The highly non-equilibrium processes produce high concentrate of Zn interstitials with different charges, including neutral, single and double. The low temperature annealing provides enough ionization energy and increases the concentration of charged Zn interstitials, strengthening the blue emissions. The high temperature annealing induces the outward diffusion of Zn interstitials and quenching of blue emissions. The following results provide several further evidences and phenomena to support such hypothesis. Additionally, the enhancement of blue emissions would benefit to the light emitting and biological fluorescence labeling applications of these ZnO nanoparticles.

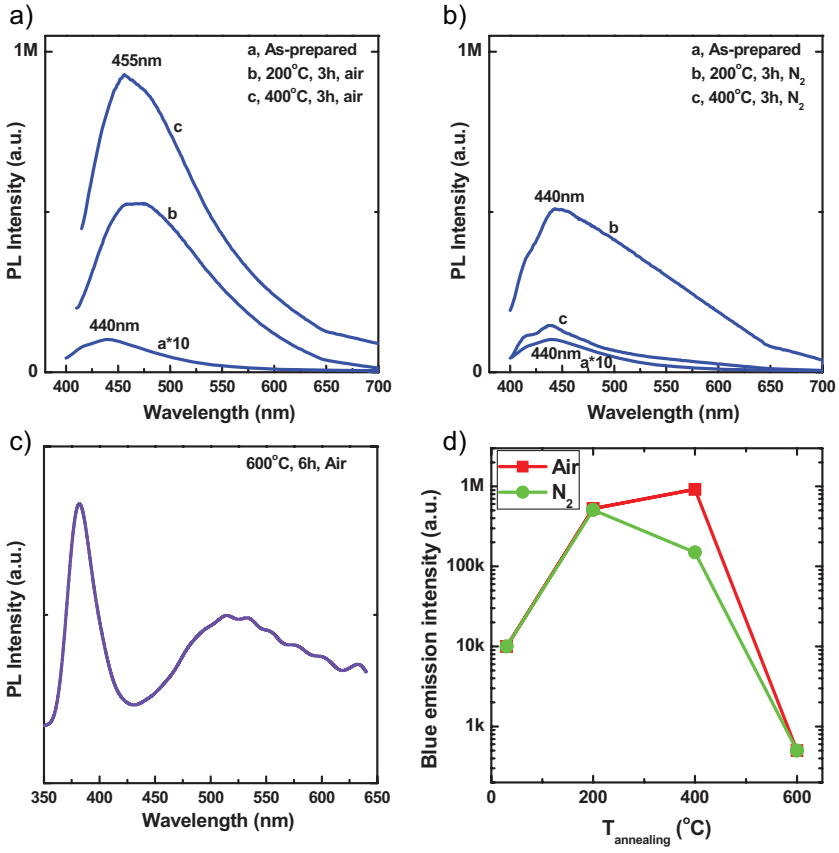

Figure 3. Blue emissions and changes with annealing in air (a) and in N_2 (b) atmosphere. c), Usual UV and green emissions after high temperature annealing. d) Intensity of blue emissions versus annealing temperature in air and N_2 atmosphere.

2.2. Excitation-Dependence and Excitation Spectra

In order to understand the features of the excited states related to these blue emissions, the PL spectra were carefully measured under different excitation energy. For the as-prepared sample (Fig. 4a), under excitation with energy much larger than the bandgap (Curve a), the spectrum exhibits two wide emission bands in blue and green regions. Two shoulders are obvious at 415 and 440 nm in the blue emission. When the excitations are selected around the bandgap (Curve b and c), the lines are unchanged in shape, with a dominant blue emission at 440 nm and a violet shoulder at 415 nm, which become strongest under the near-bandgap excitation (Curve c). The most interesting observation is that the blue

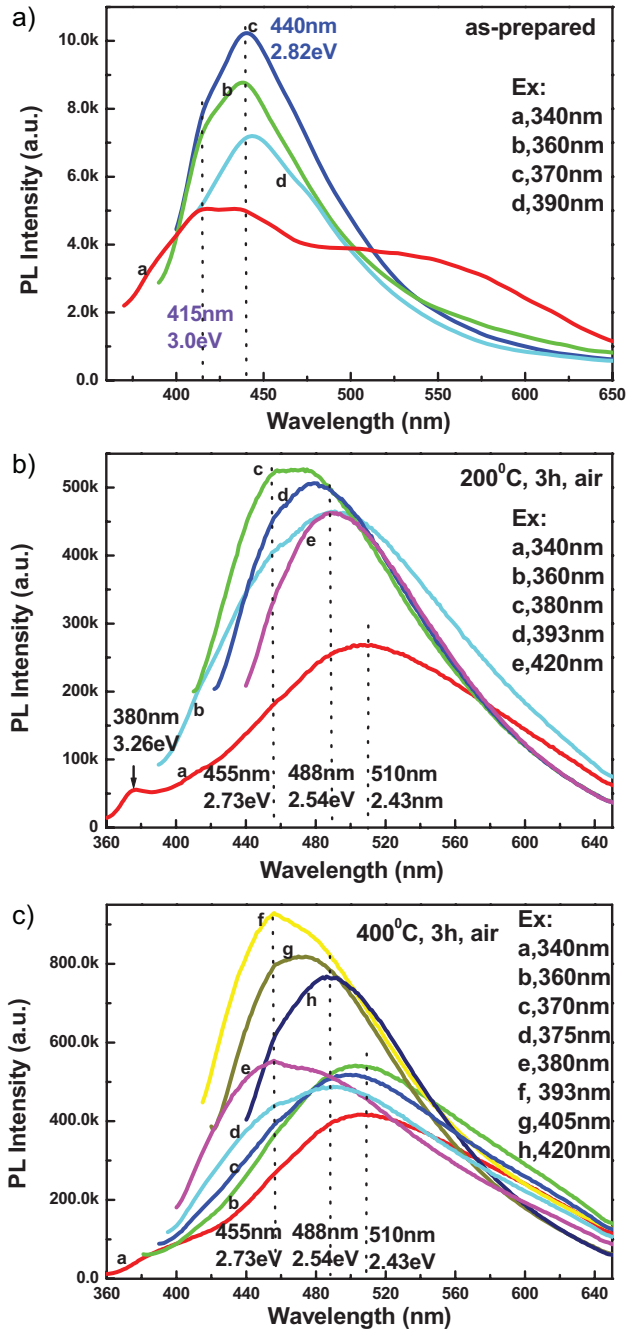

Figure 4. Excitation dependent PL of as-prepared (a), 200 °C air-annealed (b), and 400 °C air-annealed ZnO nanoparticles. The first sample shows unchanged blue emission peaks at 440 nm, but blue emission peaks slightly shifting from 455 to 488 nm in the second and third samples.

emission can also be excited by energies obviously lower than the bandgap, even with an intensity about as high as about 70% of the largest value, as shown in Curve d of Figure 4a. For the sample annealed in air, similar situations can be observed (Fig. 4b and c). The blue emissions can also be excited by energies slightly larger than the bandgap and lower than the bandgap. For example, the excitation wavelength in Curve e of Figure 4B can be as large as 420 nm with a slight decrease of emission intensity. The difference

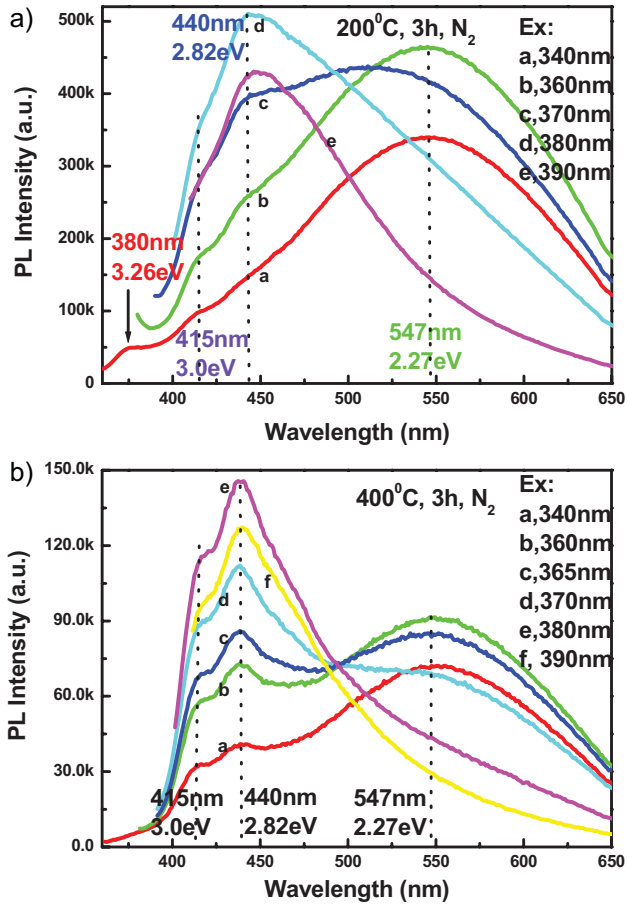

Figure 5. Excitation dependent PL of a) 200 and b) 400 °C N_2-annealed ZnO nanoparticles. In the both spectra, the blue emission peaks are fixed in 440 nm with different relative intensity of green emissions.

is that the emitting peaks seem to red-shift from 455 to 488 nm with increasing excitation wavelength. In Fig. 4c, more elaborate excitation was applied; this leads to more green emissions under above bandgap excitation. The change from green to blue emission can be well seen with increasing of excitation wavelength, as well as the intensity increasing after that.

From the samples annealed in N_2 in Figure 5, we can observe the independence of blue and green emissions. After annealing at 200 °C in N_2, the nanoparticles emit green emissions under high energy excitation (Curve a and b), but the shoulders at 415 and 440 nm are still visible. Under near-bandgap excitation (Curve c and d), the spectra change into blue emissions with a center at 440 nm. Even when the excitation energy is below the bandgap, the intensity of blue emission just reduces slightly and the peak position remains changeless, as shown in Curve e of Figure 5a. Similar phenomena can be seen from the sample annealed at 400 °C in N_2 except for the lower intensity. Moreover, these results demonstrate the significant difference between blue and green emission. Firstly, there is no continuous shift from blue to green emissions. Secondly, the green emissions can only be excited by energies larger than the bandgap, but blue emissions are preferentially excited by energies near the bandgap and obviously can still be excited by energies lower than the bandgap.

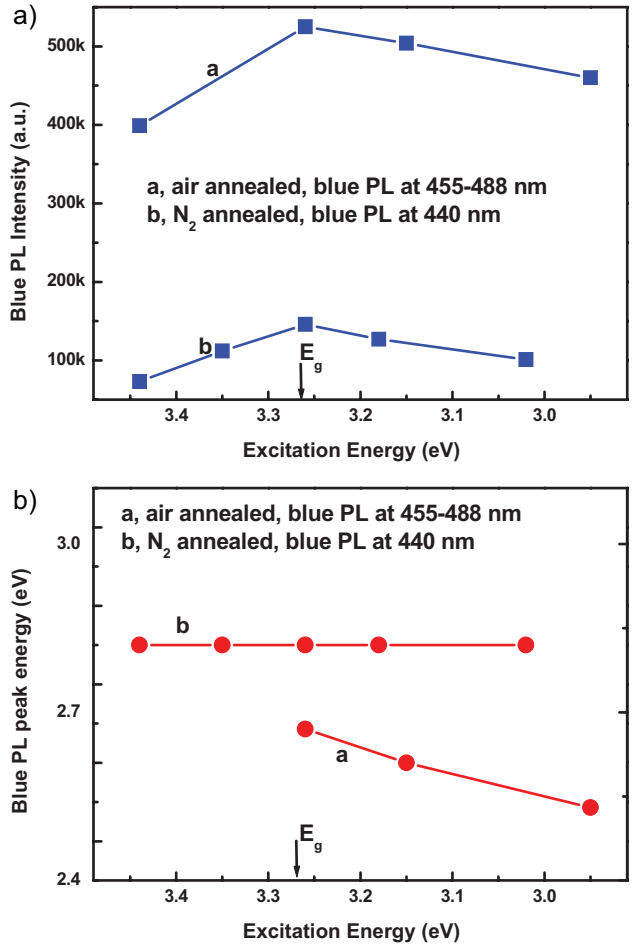

Figure 6. Changes of relative intensity and peak energy with excitation for blue emissions at 455 to 488 nm with air annealing (a), and at 440 nm with N_2 annealing (b).

Figure 6 shows the excitation dependence of blue emissions of samples, including their intensities and peak positions. The blue emissions have two significant features: 1) the intensity exhibits nonlinear increase–decrease dependence, first increasing, then reaching saturation at the bandgap energy as the optimal excitation energy, and finally decreasing but still effectively emitting at excitation energies below the bandgap energy, as shown in all of the spectra in Figure 4 and 5; and, 2) the emitting wavelengths have remarkable stability, the 440 nm emission with shoulder at 415 nm remain completely unchanged in their position, as shown in Figure 4a and 5. Even under unsuitable excitation, such as 340 nm, the positions of the corresponding shoulders are still pinned at 415 and 440 nm, as shown in Curve a in Fig. 4a and 5. As to the redshift in Figure 4b, it seems to be a feint because the blue emissions are relatively broad and there are at least two components with fixed wavelengths at 455 and 488 nm. The observed redshift is due to the disappearance of the short-wavelength component of the emission with increasing excitation wavelength. Comparatively, the green emissions can be excited only by excitation above the band-edge wavelength.

Such nonlinear intensity-dependent and stable emitting wavelengths have never been observed previously with regard to the visible emissions of ZnO. Recently, Djurišić et al. reported the monotonic quenching and blue-shift of green emissions of ZnO nanostructures with increasing excitation wavelength, and suggested that the green emissions involve transitions from shallow donor and deep acceptor levels.[58] Zhang et al. reported the monotonic quenching and red-shift of green emissions of amorphous ZnO granular films, and attributed the green emission to recombination of electrons trapped in the conduction band and deeply trapped holes in oxygen vacancies.[59] Here, the first feature of blue emissions demonstrates that the initial state of the corresponding transitions should be below the conduction band-edge. This ensures that it can effectively emit when the excitation energy is below the bandgap energy. The second feature, pinning of several emitting wavelengths, such as 415, 440, 455 and 488 nm, indicates that there could be several sub-states related to the involving defect center.

The PLE spectra of the typical green and blue emissions were measured, as shown in Figure 7. For the typical green emission, the PLE spectrum exhibits a peak at about 335 nm in the deep UV region and sharply drops at about 350 nm (Fig. 7a), indicating that the preferential excitation energy is much larger than the bandgap. Interestingly, for the 455–488 nm blue emission, the PLE spectrum shows not only a peak at energy near bandgap but also a slowly dropping tail, which continues into the violet region and contains some structuring peaks, as shown in Fig. 7b. For the 440 nm blue emission, the PLE spectra similarly exhibit a preferential excitation peak near bandgap and tail in the violet region, but the tail contains only one shoulder at about 410 nm. These PLE results are in good agreement with the above excitation-dependent PL spectra in Figure 4, 5, and 6. The flat tail extending into the violet region verifies that the initial state is located below the conduction band-edge, and the small peaks and shoulder overlapping on the tail indicate the possible sub-states of the initial state.

A detailed analysis of the initial states can be made from the defect energy level and the defect formation energy. Among the six types of point defects in ZnO lattice, V_O, Zn_i, and Zn_O are donors, while V_{Zn}, O_i, and O_{Zn} are acceptors. But, only Zn_i is a shallow donor[16,20–22,26,49] and the corresponding defect level could be located slightly below the conduction band-edge,[16,18,19,20] as revealed by many theoretical calculations and experimental results. Lin et al. calculated the energy levels of various defect centers, and pointed out that the energy gap from the interstitial zinc level to the valence band is about 2.9 eV.[60] Previously, Kroger and Bylander experimentally determined that the Zn interstitial level is 0.22 eV below the conductive band-edge.[18,55] These reported level positions are in very good agreement with the fixed violet shoulder at 415 nm (2.95 eV) in the blue emissions of this study. Look et al. observed a shallow donor with an ionization energy of 30 meV in ZnO crystal irradiated by high energy electrons, and assigned it to Zn interstitial or Zn interstitial-related complex defect.[22] In typical cases, the formation energy of Zn interstitials is very high, but it can be significantly reduced in a Zn-rich environment according to reported calculation results.[61,62] Therefore, the observed initial state could be correlated to Zn interstitials, and there could be several derivative levels with lower energies involved in localization or coupling with other defects.[44] Moreover, ZnO has a relatively open lattice structure, with tetrahedral and octahedral sites for interstitial Zn atoms. The

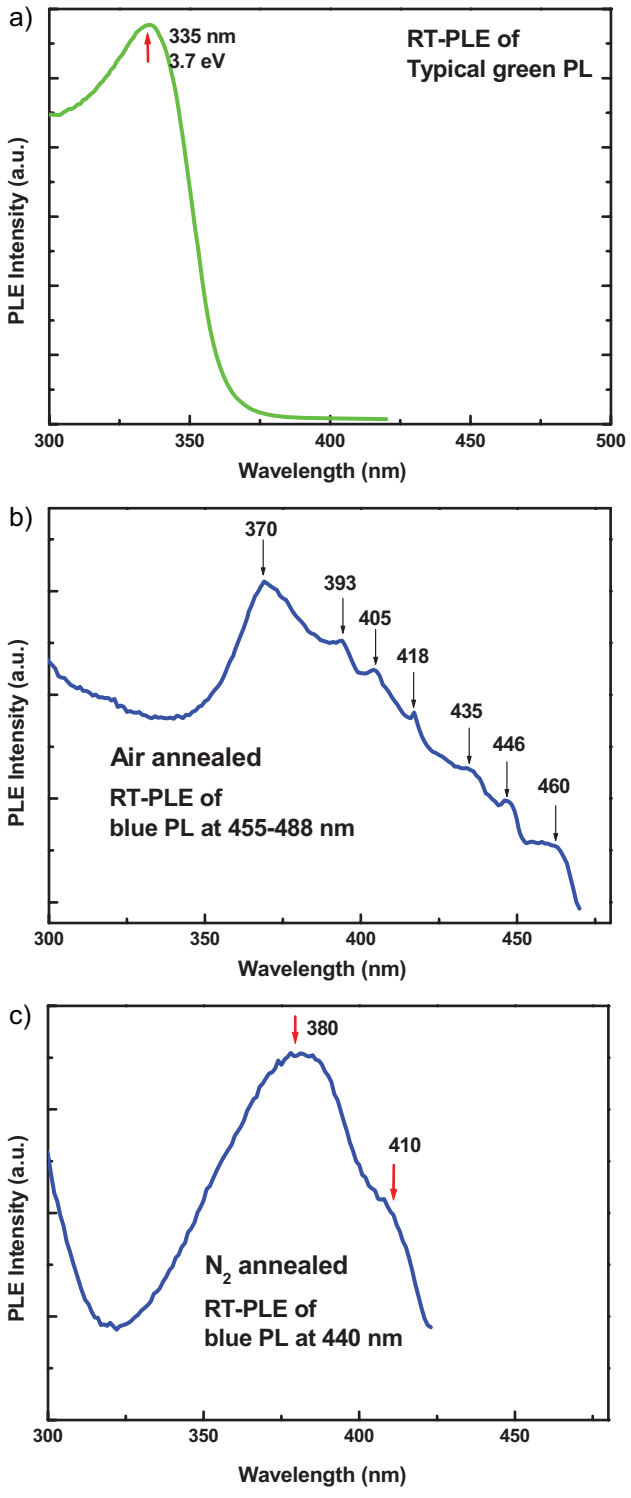

Figure 7. PLE spectra for typical green emission (a), blue emission at 455–488 nm with air annealing (b), and blue emissions at 440 nm with N_2 annealing (c).

octahedral sites are stable positions for Zn interstitials.[50] Finally, the highly non-equilibrium processes in this work will greatly advance the formation of high concentration of Zn interstitials. Recently, Halliburton et al. observed an increased concentration of free carriers in the ZnO crystal annealed in Zn vapor.[52] They attributed it to Zn intersitials being formed and also suggested that the non-equilibrium conditions are beneficial for the formation of Zn interstitials.

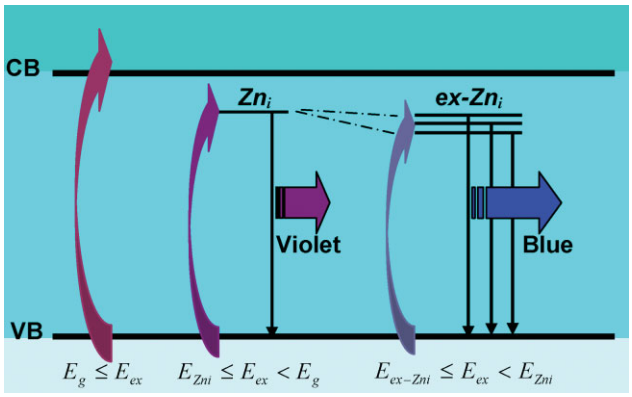

Figure 8. Proposed mechanisms of violet and blue emissions with Zn_i as the initial states.

2.3. Proposed Origins of Blue Emissions

According to the above results about excited states of blue emissions, we propose their origin to be as shown in Figure 8. The violet and blue emissions are attributed to the transitions from Zn_i and extended Zn_i states to the valance band, respectively. For the violet emission, if the electrons are excited up to a sub-band of the conduction band, they can first relax to Zn_i state through a non-radiative transition, and then transit to the valance band. According to this mechanism, two excitation modes, with $E_g \leq E_{ex}$ and $E_{Zni} \leq E_{ex} < E_g$, are effective for violet emissions. Blue emissions can be attributed to the transition from extended Zn_i states, which are slightly below the simple Zn_i state, to the valance band. These extended states can be formed during the annealing process according to the defect ionization reaction, Equation (2) and (3), and can result in defect localization coupled with a disordered lattice. According to such origins, the electrons can first transition to the conduction band or Zn_i state, then relax to extended Zn_i states, and finally transition to the valance band with blue emissions. Therefore, three excitation modes, including those with energy of $E_g \leq E_{ex}$, $E_{Zni} \leq E_{ex} < E_g$, and $E_{ex-Zni} \leq E_{ex} < E_{Zni}$, are effective for blue emissions.

These are in good agreement with the above excitation dependence results, especially that, for blue emissions, the bandgap energy is the optimal excitation energy but energies below the bandgap are still effective. Here the extended Zn_i states could be ionized Zn_i, complex defect or localized Zn_i states. More research is needed to make it clear, but a series of small peaks and shoulders in the low-energy tails in the PLE spectrum have verified their existence.

2.4. Electron Paramagnetic Resonance Spectra

One of the most powerful methods to identify the chemical nature of impurities and native defects in solid state materials is EPR spectroscopy. Because ZnO is expected to be diamagnetic, two

types of paramagnetic signals are most possible to be observed. The low-field signal with *g*-factor close to the free-electron value ($g = 2.0023$) is generally attributed to an unpaired electron trapped on an oxygen vacancy site ($g = 1.9965, 1.9948, 2.0190$ or 2.0106).[63–65] The other, high-field signal at $g = 1.96$, which has sometimes been mistakenly attributed to unpaired electrons trapped on oxygen vacancies,[25] has been reported to result from shallow donor centers.[66–69] Regardless of extrinsic impurities in ZnO, e.g., Al, Ga or In, it should be intrinsic Zn interstitials here. Moreover, Meyer and Hofmann groups identify H intersitials as a shallow donor overlapped on a Zn interstitial EPR high-field signal.[70]

The EPR spectra of as-prepared and annealed nanoparticles are presented in Figure 9. Usually, the EPR spectra of ZnO grown by the equilibrium process are smooth and narrow lines. However, the spectrum of as-prepared sample, as shown in Figure 9a, is wide and highly superimposed. This indicates that several kinds of defects are contained in the sample. The EPR signals can be separated to three components with *g*-factors of 2.01, 1.96 and 1.97, as shown by the inserted dashed lines. According to previous reports, they can be assigned to oxygen vacancies, Zn interstitials, and hydrogen interstitials from low-to high-field. Among them, Zn interstitials are the predominant defects in the as-prepared ZnO nanoparticles. This is in accord with the above analysis of the preferential formation of Zn interstitials by a highly noneqilibrium processes. Because the as-prepared sample exhibits dominant blue emissions at 440 nm, such a Zn interstitial-dominant EPR signal verifies the proposed origin based on the Zn interstitial initial state of electron transition.

With annealing, the H interstitials rapidly disappear in the all EPR spectra. This is in agreement with its high instability as predicted by theoretical works.[24,47] The coexistence of oxygen vacancies and Zn interstitials is maintained, but there emerge several significant changes, including relative ratio, intensity and width of EPR signals. The most intensive EPR signal is detected after annealing at 200 °C in air, as shown in Figure 9b. The V_O is the predominant defect in this sample. These changes demonstrate that large quantities of oxygen vacancies were formed by this annealing treatment, but Zn interstitials could still preserve a high level with relaxation. This agrees with the PL features that both green and blue emissions are relatively strong with suitable excitations and also with the stabilities of oxygen vacancies and Zn interstitials predicted by theoretical calculations;[47] therefore, this evidence also supports the proposed origins. Taking notice of the low temperature applied in annealing, it is very difficult for the external oxygen to diffuse freely into the lattice due to the insufficient drive force. Therefore, the incomplete oxidation of Zn cores inside nanoparticles would result in the formation of oxygen vacancies.[51,52] This process will accompany the relaxation of Zn interstitials. These two processes lead to the evolutions of co-existing components of oxygen vacancies and Zn interstitials.

After annealing in N_2 at 400 °C (Fig. 9C), the narrowest EPR spectrum was obtained with Zn interstitials as the dominant defects, indicating a reduction in the number of defect types. With annealing, H interstitials have completely diffused out, and the newly formed oxygen vacancies are limited because the oxidation behavior of the metal Zn cores is not obvious due to the inert atmosphere. Such EPR signals are in good agreement with the sample's PL results that the dominant emission is the fixed 440 nm blue emission, but green emissions can also be excited.

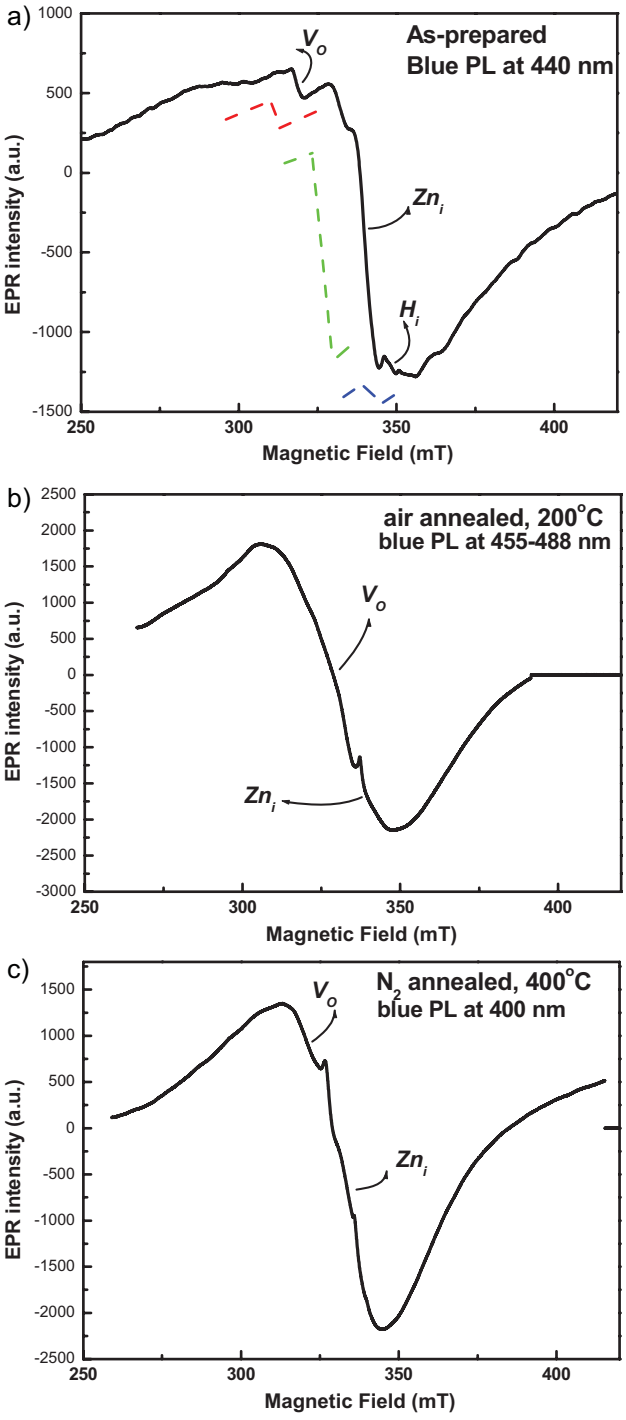

Figure 9. EPR spectra of as-prepared (a), air-annealed (b) and N_2-annealed (c) ZnO nanoparticles. The EPR signals exhibit coexistence of Zn_i and V_O, and changes of intensity, width, and relative component ratio.

2.5. Further Controls of Co-Emitting and Peak-Shift

The above results demonstrate that the defect states can be adjusted by low temperature annealing, and the proposed mechanisms suggest that the excited states can also be adjusted

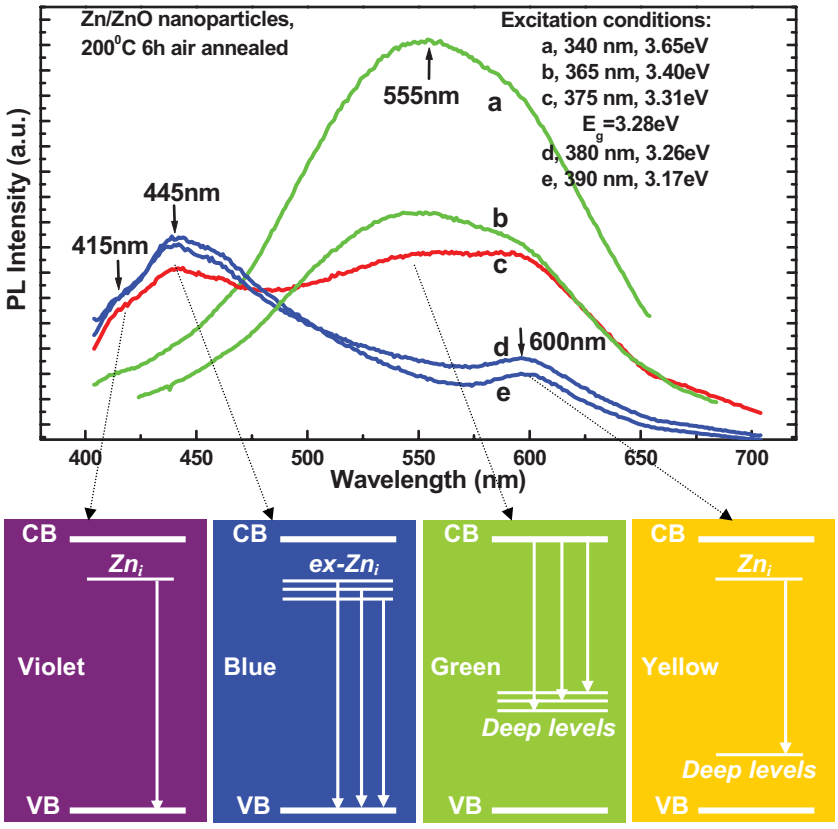

Figure 10. Excitation-dependent PL spectra of 200 °C air-annealed nanoparticles, displaying controllable selection and co-emission of visible emissions. The proposed mechanisms are denoted for violet, blue, green, and yellow emissions, respectively.

by selection of the excitation energy. Therefore, combining the selection of annealing and excitation should be effective for the control of blue emissions of ZnO nanoparticles.

Figure 10 shows the PL spectra of samples annealed at 200 °C in air and under various excitations. When the excitation energy is larger than E_g, the PL spectra (Curve a and b) exhibit a broad green emission with center at 555 nm and a shoulder at yellow region. The Gaussian fitting in Figure 11a clearly shows two sub-bands in the green and yellow regions. With the excitation energy decreasing, the green emission weakens but a new blue emission, with center at 445 nm, emerges and increases. When the excitation energy is near the bandgap, a very broad emission can be obtained, as shown in Curve c, in which the blue and green emissions have comparable intensity, forming a homogenous emission from around 400 to 600 nm. Interestingly, the corresponding fitting in Figure 11b presents five comparable emissions with centers at 417, 440, 472, 527, and 590 nm. This phenomenon indicates the co-emission of transitions involving different defects. As the excitation energy decreases below the bandgap, most of the green emission is quenched except for a weak shoulder at 600 nm, and the spectra are dominated by the blue emission with changeless peak position, as shown in Curve d and e, and this can be described well by the Gaussian fitting in Figure 11c.

The selection and co-emission of different visible emissions can be well interpreted according to the above-proposed mechanisms, as shown in the four inserted schemes in Figure 10. When the energy of the incident photons is just enough to pump the electrons up to the Zn_i energy level but not to the conductance band, a mass of electrons can be directly trapped by the Zn_i defect centers, which will induce effective transitions from the Zn_i energy level to the valance band and other deep levels, inducing violet, blue and yellow emissions according to the energy differences. These three types of emission can all emit with below-E_g excitation. In contrast, green emission is usually only efficient under the above-E_g excitation, thus suggesting it to be from the transition from the conduction band to deep levels. This agrees with many previous reports. As to the cooperative emission of multiple colors, this is the result of the coexistence of several types of defects and suitable excitations according to the proposed origins. This indicates that more elaborate annealing can be expected to enable controlled co-emission in the visible region.

This provides an method combining annealing and excitation to control these polychromic visible emissions of nanostructured ZnO, including single band, multi-band and large-region homogeneous emissions, exhibiting different monochromes and mixed colors, even including white. Along these lines, elaborate annealing and excitation were carried out in pursuit of more visible emissions. The spectra and corresponding conditions are presented in Figure 12. A series of relatively homochromous visible emissions can be obtained with centers from 440 to 555 nm. Such abundant adjustments will greatly benefit the applications of ZnO nanoparticles in light emission, display devices, biological labeling, and so on.

These results point to an interesting issue: some key properties of ZnO depend not only on intrinsic parameters, such as the crystal structure, bulk composition and morphology, but also on the type and number of defects. Therefore, it is necessary to control not only the composition and morphology but also the defect structure for nanostructures.

3. Conclusions

1. Highly defective nanocrystalline ZnO can be prepared far from thermodynamic equilibrium, for example, by laser ablation in liquid with local extreme conditions of high temperature, high pressure and high concentration of highly excited species, and subsequent zinc-rich annealing. This assumption is in good agreement with recent theoretical calculation of thermodynamic stability of defects in ZnO.
2. The presence of defects formed in highly non-equilibrium conditions had a significant impact on the luminescence of ZnO. These ZnO nanoparticles exhibit very strong blue emissions, the intensity of which first increases and then decreases with annealing. Significantly, strong and interesting excitation-

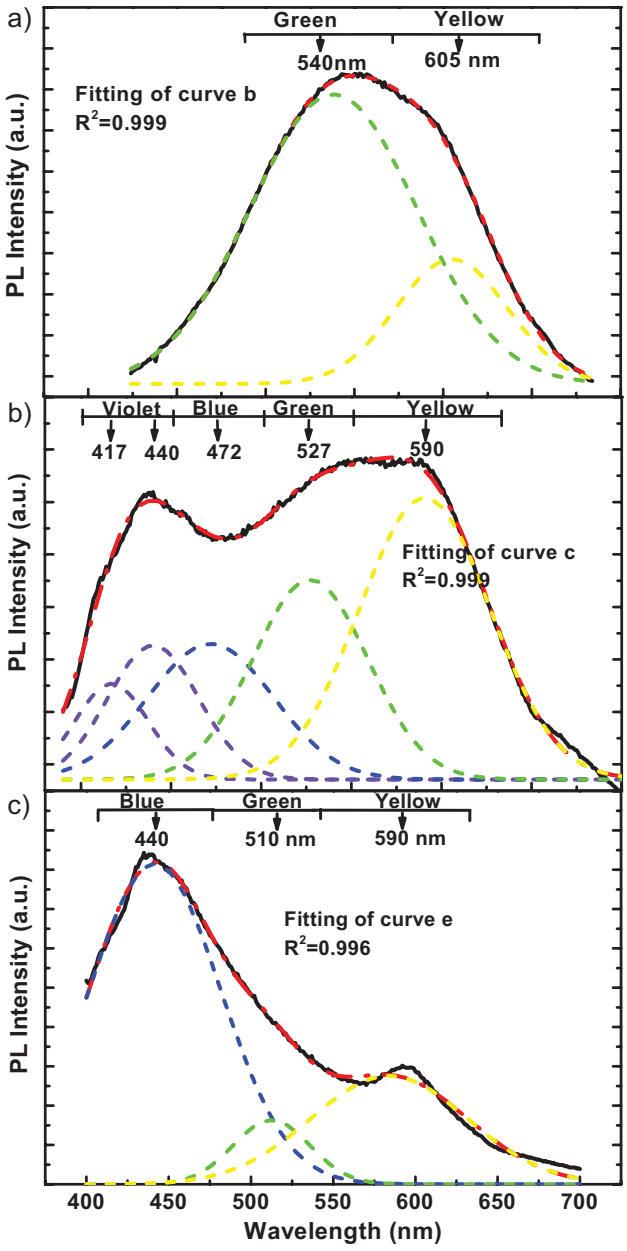

Figure 11. Gaussian fitting curves of green (a), blue-green (b), and blue (c) emissions, exibiting several sub-bands with similar peak positions to those observed in excitation-dependent PL spectra.

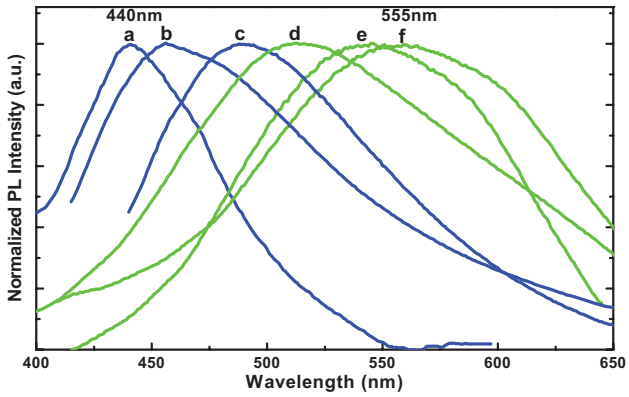

Figure 12. Normalized visible emissions of ZnO nanoparticles with controllable peak positions from blue to green regions.

Table 1. Annealing and excitation conditions applied for controllable emissions in Figure 12.

Sample	Conditions	Excitation [nm]	Emission [nm]
a	As-prepared	370	440
b	Air 400 °C 3 h	370	455
c	Air 400 °C 3 h	420	488
d	Air 400 °C 3 h	340	510
e	Air 300 °C 6 h	340	545
f	Air 200 °C 6 h	340	555

dependence was observed for these visible emissions for the first time: 1) the optimal excitation energy for blue emissions is near the bandgap energy, but the effective excitation can obviously be less than it, while green emissions can be excited only by energies larger than bandgap energy; and, 2) there are several fixed emission wavelengths at 415, 440, 455 and 488 nm for the blue emissions.

3. Combined with reported defect energy levels and formation thermodynamics, the origins of the defect state of Zn_i and derivative extended states as initial states for electron transitions are proposed. EPR spectra revealed the predominance of Zn_i in as-prepared samples, and the changes of coexisting Zn_i and oxygen vacancies with annealing. These EPR results further verify the proposed origins.
4. Furthermore, according to the observed phenomena and built mechanisms, good controllability was achieved, including the co-emission of blue and green emissions, and adjustment of the emitting wavelength from blue to green regions.
5. The completely different behavior of green emissions in excitation dependence PL and EPR provide support that it originated from the transition from the conduction band to deep defect levels.

This work provides information towards the final clarification of the origins of defect-related emissions in ZnO nanostructures, and extends the optical and electronic applications of nanostructured ZnO. What becomes obvious from these findings is that control of morphology (i.e., "size and shape") and composition is not sufficient for materials at the nanoscale. Controlling materials properties, which is the highest goal of contemporary nanotechnology, needs to involve the control of defects as well.

4. Experimental

Laser Ablation in Liquid Synthesis: The laser ablation of a zinc target is performed in an aqueous solution with sodium dodecyl sulfate (SDS), as previously reported in detail elsewhere [43,44]. Briefly, A zinc plate

(99.99%) was fixed on a bracket in a glass vessel filled with 10 mL SDS (99.5%) aqueous solution (0.05 M). The plate was ablated (irradiated) for 30 min by the first harmonic of a Nd:YAG laser (1 064 nm, frequency 10 Hz, pulse duration 10 ns) with power 70 mJ pulse^{-1}. The laser beam was focused on the metal plate with a beam size of about 2 mm in diameter using a lens with a focal length of 150 mm.

Annealing of Nanoparticles: After synthesis by laser ablation, all of the colloidal suspensions were centrifuged at 14 000 rpm, ultrasonically rinsed with ethanol at least five times, and air dried in an oven at 40 °C. Some obtained powder products were annealed in a tube-type stove with program-controlled temperature and different atmospheres.

Characterizations: The obtained samples were characterized by x-ray diffraction (XRD, Philips X'Pert with Cu Kα line of 0.15419 nm), transmission electron microscopy (TEM, JEM-200CX), and high resolution transmission electron microscopy (HRTEM, JEOL-2010). The PL and PLE spectra were measured using He-Cd laser excitation (wavelength 325nm) at room temperature and Xe lamp excitation (Edinburgh luminescence spectrometer FLS 920) with different excitation wavelengths at different temperatures. The electron paramagnetic resonance (EPR) measurement was conducted on an EPR-200 spectrometer using an X band (9.65 GHz).

Acknowledgements

This work was financially supported by the National Natural Science Foundation of China (grant nos. 10604055 and 50671100), the Major State Research Program of China "Fundamental Investigation on Micro-Nano Sensors and Systems based on BNI Fusion" (grant no. 2006CB300402), and the Knowledge Innovation Program of the Chinese Academy of Sciences (grant no. KJCX2-SW-W31).

Received: October 6, 2009
Published online: January 11, 2010

[1] W. Park, G. Yi, *Adv. Mater.* **2004**, *16*, 87.
[2] H. K. Fu, C. L. Cheng, C. H. Wang, T. Y. Lin, Y. F. Chen, *Adv. Funct. Mater.* **2009**, *19*, 1.
[3] Y. Qin, X. Wang, Z. L. Wang, *Nature* **2008**, *451*, 809.
[4] H. B. Zeng, W. P. Cai, P. S. Liu, X. X. Xu, H. J. Zhou, C. Klingshirn, H. Kalt, *ACS Nano.* **2008**, *2*, 1661.
[5] H. B. Zeng, X. J. Xu, Y. Bando, U. K. Gautam, T. Y. Zhai, X. S. Fang, B. D. Liu, D. Golberg, *Adv. Funct. Mater.* **2009**, *19*, 3165.
[6] G. Z. Shen, Y. Bando, B. Liu, D. Golberg, C. Lee, *Adv. Funct. Mater.* **2006**, *16*, 410.
[7] M. H. Huang, S. Mao, H. Feick, H. Q. Yan, Y. Y. Wu, H. Kind, E. Weber, R. Russo, P. D. Yang, *Science* **2001**, *292*, 1897.
[8] H. J. Zhou, J. Fallert, J. Sartor, R. J. B. Dietz, C. Klingshirn, H. Kalt, D. Weissenberger, D. Gerthsen, H. B. Zeng, W. P. Cai, *Appl. Phys. Lett.* **2008**, *92*, 132112.
[9] A. Tsukazaki, A. Ohtomo, T. Onuma, M. Ohtani, T. Makino, M. Sumiya, K. Ohtanis, S. Chichibu, S. Fuke, Y. Segawa, H. Ohno, H. Koinuma, M. Kawasaki, *Nat. Mater.* **2005**, *4*, 42.
[10] B. Xiang, P. W. Wang, X. Z. Zhang, S. A. Dayeh, D. P. R. Aplin, C. Soci, D. P. Yu, D. L. Wang, *Nano. Lett.* **2007**, *7*, 323.
[11] G. D. Yuan, W. J. Zhang, J. S. Jie, X. Fan, J. A. Zapien, Y. H. Leung, L. B. Luo, P. F. Wang, C. S. Lee, S. T. Lee, *Nano. Lett.* **2008**, *8*, 2591.
[12] U. K. Gautam, L. S. Panchakarla, B. Dierre, X. Fang, Y. Bando, T. Sekiguchi, A. Govindaraj, D. Golberg, C. N. R. Rao, *Adv. Funct. Mater.* **2009**, *19*, 131.
[13] P. Sharma, A. Gupta, K. V. Rao, F. J. Owens, R. Sharma, R. Ahuja, J. M. O. Guillen, B. Johansson, G. A. Gehring, *Nat. Mater.* **2003**, *2*, 673.
[14] Ü. Özgür, Y. Alivov, C. Liu, A. Teke, M. Reshchikov, S. Dogan, V. Avrutin, S. Cho, H. Morkoc, *J. Appl. Phys.* **2005**, *98*, 041301.
[15] L. Schmide-Mende, J. L. MacManus-Driscoll, *Mater. Today* **2007**, *10*, 40.
[16] K. I. Hagemark, L. C. Chacha, *J. Solid State Chem.* **1975**, *15*, 261.
[17] G. D. Mahan, *J. Appl. Phys.* **1983**, *54*, 3825.
[18] F. A. Kröger, *The Chemistry of Imperfect Crystals*, 2nd Ed. North Holland, Amsterdam **1974**.
[19] V. Gavryushin, G. Račiukaitis, D. Juodžbalis, A. Kazlaulskas, V. Kubertivičius, *J. Cryst. Growth* **1994**, *138*, 924.
[20] D. C. Look, J. W. Hemsky, *Phys. Rev. Lett.* **1999**, *82*, 2552.
[21] F. Tuomisto, V. Ranki, K. Saarinen, D. C. Look, *Phys. Rev. Lett.* **2003**, *91*, 205502.
[22] D. C. Look, G. C. Falow, P. Reunchan, S. Limpijumnong, S. B. Zhang, K. Nordlund, *Phys. Rev. Lett.* **2005**, *95*, 225502.
[23] C. G. Van de Walle, *Phys. Rev. Lett.* **2000**, *85*, 1012.
[24] A. Janotti, C. G. Van de Walle, *Nat. Mater.* **2007**, *6*, 44.
[25] K. Vanheusden, C. H. Seager, W. L. Warren, D. R. Tallant, J. A. Voigt, *Appl. Phys. Lett.* **1996**, *68*, 403.
[26] S. B. Zhang, S. H. Wei, A. Zunger, *Phys. Rev. B* **2001**, *63*, 075205.
[27] H. S. Kang, J. S. Kang, J. W. Kim, S. Y. Lee, *J. Appl. Phys.* **2004**, *95*, 1246.
[28] R. Dingle, *Phys. Rev. Lett.* **1969**, *23*, 579.
[29] R. E. Dietz, H. Kamimura, M. D. Sturge, A. Yariv, *Phys. Rev.* **1963**, *132*, 1559.
[30] B. M. Kimpel, H. J. Schulz, *Phys. Rev. B* **1991**, *43*, 9938.
[31] S. A. Studenikin, N. Golego, M. Cocivera, *J. Appl. Phys.* **1998**, *84*, 2287.
[32] F. H. Leiter, H. R. Alves, N. G. Romanov, D. M. Hofmann, B. K. Meyer, *Phys. B (Amsterdam, Neth.)* **2003**, *340–342*, 201.
[33] N. O. Korsunska, L. V. Borkovska, B. M. Bulakh, L. V. Khomenkova, V. I. Kushnirenko, I. V. Markevich, *J. Lumin.* **2003**, *102*, 733.
[34] F. Oba, S. R. Nishitani, S. Isotani, H. Adachi, *J. Appl. Phys.* **2001**, *90*, 824.
[35] Y. F. Yan, S. B. Zhang, *Phys. Rev. Lett.* **2001**, *86*, 5723.
[36] C. H. Park, S. B. Zhang, S. H. Wei, *Phys. Rev. B* **2002**, *66*, 073202.
[37] Y. H. Yang, X. Y. Chen, Y. Feng, G. W. Yang, *Nano. Lett.* **2007**, *7*, 3879.
[38] N. W. Wang, Y. H. Yang, G. W. Yang, *J. Phys. Chem. C* **2009**, *113*, 15480.
[39] A. B. Djurišić, Y. H. Leung, *Small* **2006**, *2*, 944.
[40] H. B. Zeng, W. P. Cai, J. L. Hu, G. T. Duan, P. S. Liu, Y. Li, *Apply. Phys. Lett.* **2006**, *88*, 171910.
[41] H. B. Zeng, Z. G. Li, W. P. Cai, P. S. Liu, *J. Appl. Phys.* **2007**, *102*, 104307.
[42] J. J. Wu, S. C. Liu, *Adv. Mater.* **2002**, *14*, 215.
[43] H. B. Zeng, W. P. Cai, Y. Li, J. L. Hu, P. S. Liu, *J. Phys. Chem. B* **2005**, *109*, 18260.
[44] H. B. Zeng, Z. G. Li, W. P. Cai, B. Q. Cao, P. S. Liu, S. K. Yang, *J. Phys. Chem. B* **2007**, *111*, 14311.
[45] P. P. Patil, D. M. Phase, S. A. Kulkarni, S. V. Ghaisas, S. K. Kulkarni, S. M. Kanetkar, S. B. Ogale, V. G. Bhide, *Phys. Rev. Lett.* **1987**, *58*, 238.
[46] K. I. Hagemark, *J. Solid State Chem.* **1976**, *16*, 293.
[47] V. Ischenko, S. Polarz, D. Grote, V. Stavarache, K. Fink, M. Driess, *Adv. Funct. Mater.* **2005**, *15*, 1945.
[48] F. Tuomisto, V. Ranki, K. Saarinen, *Phys. Rev. Lett.* **2003**, *91*, 205502.
[49] L. S. Vlasenko, G. D. Watkins, *Phys. Rev. B* **2005**, *72*, 035203.
[50] A. Janotti, C. G. Van de Walle, *Phys. Rev. B* **2007**, *76*, 165202.
[51] J. P. Han, P. Q. Mantas, A. M. R. Senos, *J. Eur. Ceram. Soc.* **2002**, *22*, 49.
[52] L. E. Halliburton, N. C. Giles, N. Y. Garces, M. Luo, C. C. Xu, L. H. Bai, L. A. Boatner, *Appl. Phys. Lett.* **2005**, *87*, 172108.
[53] G. W. Tomlins, J. L. Routbort, T. O. Mason, *J. Appl. Phys.* **2000**, *87*, 117.
[54] B. J. Wuensch, H. L. Tuller, *J. Phys. Chem. Solids* **1994** *55*, 975.
[55] E. G. Bylander, *J. Appl. Phys.* **1978**, *49*, 1188.
[56] W. H. Zhang, J. L. Shi, L. Z. Wang, S. S. Yan, *Chem. Mater.* **2000**, *12*, 1408.
[57] X. H. Zhang, S. Y. Xie, Z. Y. Jiang, X. Zhang, Z. Q. Tian, Z. X. Xie, R. B. Huang, L. S. Zheng, *J. Phys. Chem. B* **2003**, *107*, 10114.
[58] A. B. Djurišić, Y. H. Leung, K. H. Tam, L. Ding, W. K. Ge, H. Y. Chen, S. Gwo, *Appl. Phys. Lett.* **2006**, *88*, 103107.
[59] W. C. Zhang, X. L. Wu, H. T. Chen, J. Zhu, G. S. Huang, *J. Appl. Phys.* **2008**, *103*, 093718.
[60] B. X. Lin, Z. X. Fu, Y. B. Jia, *Appl. Phys. Lett.* **2001**, *79*, 943.
[61] P. Erhart, K. Albe, A. Klein, *Phys. Rev. B* **2006**, *73*, 205203.
[62] A. F. Kohan, G. Ceder, D. Morgan, C. G. Van de Walle, *Phys. Rev. B* **2000**, *61*, 15019.

[63] N. G. Kakazev, T. V. Sreckovic, M. M. Ristic, *J. Mater. Sci.* **1997**, *32*, 4619.
[64] B. Yu, C. Zhu, F. Gan, Y. Huang, *Mater. Lett.* **1998**, *33*, 247.
[65] L. Jing, Z. Xu, J. Shang, X. Sun, W. Cai, H. Guo, *Mater. Sci. Eng. A* **2002**, *322*, 356.
[66] M. Schulz, *Phys. Status Solidi A* **1975**, *27*, K5.
[67] D. Block, A. Herve, R. T. Cox, *Phys. Rev. B* **1982**, *25*, 6049.
[68] C. Gonzales, D. Block, R. T. Cox, A. Herve, *J. Cryst. Growth* **1982**, *59*, 357.
[69] N. Y. Garces, L. Wang, L. Bai, N. C. Giles, L. E. Halliburton, G. Cantwell, *Appl. Phys. Lett.* **2002**, *81*, 622.
[70] D. M. Hofmann, A. Hofstaetter, F. Leiter, H. Zhou, F. Henecker, B. K. Meyer, S. B. Orlinskii, J. Schmidt, P. G. Baranov, *Phys. Rev. Lett.* **2002**, *88*, 045504.